RSC Advances

ROYAL SOCIETY OF CHEMISTRY

PAPER

View Article Online
View Journal | View Issue

Cite this: *RSC Adv.*, 2026, **16**, 11864

Thermochemically activated *Ficus benghalensis* leaf-derived porous activated carbon for sustainable supercapacitor electrodes

Balanagouda N. Choudari, †[a] Shreeganesh Subraya Hegde, †*[bc] Mervin A. Herbert,[a] Kumar G. N.[a] and Badekai Ramachandra Bhat *[b]

The adoption of renewable energy for mitigating climate change has intensified the demand for energy storage solutions. Embracing the circular economy, the valorisation of agricultural or forest biomass into electrode materials for energy storage systems provides a sustainable and environmentally friendly pathway. Herein, we synthesised an electrode material from dead *Ficus benghalensis* (Banyan tree) leaves by a thermochemical activation process at 700 °C. Systematic structural and morphological characterisation of the resulting *Ficus benghalensis* leaf-derived activated carbon (BLC_KOH) exhibited a hierarchical porous structure with a specific surface area of 495.56 $m^2\ g^{-1}$. Electrochemical measurements of the BLC_KOH electrode performed in Na_2SO_4 (1 M) electrolyte in a two-electrode symmetric configuration demonstrated a specific capacitance of 561.22 F g^{-1} at a current density of 0.2 A g^{-1}. Surface-controlled charge storage was found to be the dominant mechanism at a scan rate of 100 mV s^{-1} based on Dunn analysis. Exceptional cycling stability with ∼99.99% capacity retention was shown even after 1000 cycles, demonstrating its strong potential as a next-generation energy-storage electrode material. This study demonstrates that *Ficus benghalensis* leaves can serve as an abundant and renewable precursor for electrode materials, offering a pathway for sustainable and eco-friendly energy storage solutions.

Received 12th December 2025
Accepted 12th February 2026

DOI: 10.1039/d5ra09628f

rsc.li/rsc-advances

1 Introduction

The growing embrace of renewable energy sources has fostered the global shift towards a future of sustainable energy, which is exerting an unprecedented demand for innovative energy storage solutions.[1] Although solar and wind energies are promising clean energy sources, their fluctuating output hampers grid performance, which necessitates a strong energy storage infrastructure.[2,3] Traditionally, batteries are a promising solution, but their limitations in delivering high power density and long cycle life requirements have opened the door for complementary technologies. Thus, supercapacitors, with their promising abilities, have emerged as the best fit for the evolving landscape.[4]

Supercapacitors are specifically used in applications that demand instantaneous power supply and involve very high charge–discharge cycles, and these requirements cannot be met by conventional batteries.[5] Among their various applications, the transportation sector holds a major share due to the adoption of electric vehicles (EVs). Electric vehicles use supercapacitors to capture and store braking energy, provide rapid power during acceleration, thereby reducing strain on the main battery pack. Additionally, the ability of supercapacitors to perform at low temperatures helps to improve the responsiveness and reliability of EV vehicles.[6,7] In manufacturing and automation systems, they are used to start high-torque motors and actuators, maintain emergency stop functionality during breakdown and store energy from decelerating machinery, thereby improving system efficiency.[8] Their critical roles in high-power applications, fast-charging systems, and high-cycle applications drive the growth and technological advancement in the energy storage ecosystem.

The development of electrode materials has undergone a significant evolution over time. Initially, research was centered on producing activated carbon through straightforward physical and chemical activation techniques. A subsequent paradigm shift led to the exploration of high-performance metal oxides, notably using sol–gel synthesis to create materials like ruthenium oxide and other transition-metal oxides. The discovery of carbon nanotubes in 1991[9] marked a major turning point, which introduced high-surface-

---

[a] *Department of Mechanical Engineering, National Institute of Technology Karnataka, Surathkal, Mangalore, Karnataka 575025, India*

[b] *Catalysis and Materials Chemistry Laboratory, Department of Chemistry, National Institute of Technology Karnataka, Surathkal, Mangalore, Karnataka 575025, India. E-mail: hegdeshreeganesh@gmail.com; ram@nitk.edu.in*

[c] *Department of Chemistry, School of Engineering, Dayananda Sagar University, Horahalli, Bengaluru, Karnataka 562112, India*

† BNC and SSH contributed equally to this work.

area electrode materials with exceptional performance for energy storage applications. This was followed by the groundbreaking discovery of graphene in 2004,[10] which accelerated and paved the way for development of advanced two-dimensional materials such as MXenes.[11] In the current landscape, influenced by the principles of green chemistry, there is a growing emphasis on developing sustainable electrode materials derived from biomass.

In the journey from waste to energy storage (bio-inspired electrode materials), many waste or unutilised biomass resources are tapped to prepare activated carbon. Among the great wealth of biomass resources, this research reports the preparation of activated carbon from banyan tree leaves. *Ficus benghalensis*, commonly known as the banyan tree, is indigenous to the Indian subcontinent. Its main feature is its extensive canopy, which can spread across a large area, supported by its aerial roots that later develop into thick, woody trunks. The large oval or elliptical leaves have a lignocellulosic composition that is optimal as a primary precursor for activated carbon.[12,13] In this study, *Ficus benghalensis* leaves were transformed into highly porous activated carbon for supercapacitor electrodes through a carbonisation and KOH chemical activation strategy. The physicochemical properties of the resulting material were obtained from characterisation techniques such as XRD, Raman and FTIR spectroscopy, EDX, FESEM, XPS, and N_2 adsorption–desorption analysis. Its electrochemical performance was evaluated by conducting cyclic voltammetry (CV), galvanostatic charge–discharge (GCD) analysis and electrochemical impedance spectroscopy (EIS) in a two-electrode symmetric configuration.

2 Experimental study

2.1 Materials

Naturally fallen leaves of *Ficus benghalensis* (banyan tree) were stockpiled from the campus of the National Institute of Technology Karnataka, and used as a precursor to develop the activated carbon material. Potassium hydroxide pellets (KOH) and hydrochloric acid (HCl) were sourced from Loba Chemie Pvt. Ltd. Ethanol (absolute) was procured from Changshu Hongsheng Fine Chemicals. Potassium phosphate monobasic (H_2KO_4P), polyvinylidene fluoride (PVDF), and *N*-methyl-2-pyrrolidone (NMP) were procured from Sigma-Aldrich. C-NERGY SUPER C65 carbon black (TIMCAL) and Grafoil sheets were used as received. Ultrapure water (Type 1) was used to prepare all the solutions.

2.2 Synthesis of banyan tree leaf-derived activated carbon (BLC)

Naturally fallen *Ficus benghalensis* leaves were collected, thoroughly rinsed with ultrapure water, and sun-dried for a week before being pulverized into a fine powder. The pulverised biomass was homogeneously mixed with potassium phosphate monobasic (H_2KO_4P) in a ratio of 1 : 1 (w/w) using ultrapure water as the medium. The resulting slurry underwent thermal treatment under continuous stirring until a paste formed. The dried paste was subjected to carbonization in a tube furnace under an argon gas atmosphere at 450 °C for 30 minutes. The carbonized sample was subjected to different procedures to obtain two types of activated carbon. The first type of activated carbon material was synthesised by pyrolyzing the sample at 700 °C for 30 minutes at a ramp rate of 20 °C min^{-1} under a constant argon gas flow rate of 150 mL min^{-1}. The second type of activated carbon material was synthesised by impregnation with aqueous KOH solution in a 1 : 1 ratio, followed by thermal treatment under continuous stirring to yield a homogeneous paste. The paste underwent pyrolysis at 700 °C for 30 minutes under argon flow. After pyrolysis, both materials were subjected to identical post-synthesis purification. The purification steps involved treating with 30% HCl solution to eliminate inorganic and other impurities, followed by washing with ultrapure water to achieve neutral pH. The final step involved rinsing with ethanol and drying in an oven at 110 °C for 24 hours. The resulting material was named as BLC and BLC_KOH and stored in a desiccated environment before characterisation.

2.3 Structural and morphological characterisation

Thermal gravimetric analysis (TGA) and derivative thermogravimetry (DTG) were carried out in TGA 4000 at a heating ramp of 10 °C min^{-1} to determine the thermal stability of the material. X-ray diffraction studies were performed with an Empyrean 3rd Gen, Malvern Panalytical (Netherlands) instrument, with a Cu-Kα source with a wavelength of 0.154 nm, to determine the structural characteristics of the materials. Further confirmation of the structural properties was obtained by Raman spectroscopy using a confocal Raman microscope (Renishaw, UK) with an excitation wavelength of 532 nm. The morphologies of the samples were analysed using HR-FESEM (GEMINI 300, Carl Zeiss, Germany), and the elemental composition was obtained by energy-dispersive X-ray (EDX) analysis. FTIR studies were conducted with a Spectrum 2 FT-IR Spectrometer (PerkinElmer, Singapore), and XPS was performed to establish the presence of various functional groups. N_2 adsorption–desorption measurements (Autosorb IQ-XR-XR, Anton Paar, Austria) were conducted to analyse the sample's pore size distribution and specific surface area by outgassing the samples under vacuum for 3 hours at 300 °C.

2.4 Electrode fabrication and electrochemical evaluation of BLC_KOH

The working electrode was fabricated by grinding the active material (80 wt%), C65 (10 wt%), and PVDF binder (10 wt%) in NMP solvent. The homogenised black paste was uniformly drop-casted on the Grafoil substrate (1 cm^2), yielding electrodes with an active loading mass of 2 mg cm^{-2}. The electrode was further processed under vacuum conditions at 60 °C overnight. The electrochemical performance of the resulting electrode was measured in a symmetric electrode configuration with filter paper as a separator in 1 M Na_2SO_4 as the electrolyte. With an Autolab electrochemical workstation, cyclic voltammetry and galvanostatic charge–discharge were conducted in a potential window of 0–1 V at scan rates of 5 mV s^{-1} to 100 mV s^{-1} and a current density from 0.2 A g^{-1} to 1 A g^{-1}, respectively. EIS was conducted in the frequency range of 0.01 Hz to 1 MHz with an amplitude of 10 mV. The electrochemical performance parameters were calculated from the following equations:[14]

$$\text{Specific capacitance }\left(C_{\text{sp}}, \text{F g}^{-1}\right) = 2 \times \frac{I}{m} \times \left(\frac{\Delta t}{\Delta V}\right)$$

$$\text{Energ density}\left(E_{\text{d}}, \text{Wh kg}^{-1}\right) = \frac{1}{2 \times 3.6} \times C_{\text{sp}}(\Delta V)^2$$

$$\text{Power density}\left(P_{\text{d}}, \text{W kg}^{-1}\right) = \frac{3600 \times E_{\text{d}}}{t}$$

where ΔV, I, Δt, and m are the potential change within Δt, the current (A), the discharge time (s), and the active material loading mass (g), respectively.

3 Results and discussion

3.1 Physicochemical characterisation

Thermogravimetric analyses (TGA, argon (Ar) atmosphere, heat rate = 10 °C min^{-1}) and derivative thermogravimetry (DTG) were carried out on the precursor material after pulverisation. The multi-step thermal decomposition is observed in Fig. 1a. The initial weight loss can be attributed to moisture loss up to 110 °C. The second stage of decomposition involves rapid weight loss from ~175 °C to ~420 °C, which is confirmed by a DTG minima at ~320 °C. This stage can be attributed to the breakdown of cellulose and hemicellulose present in the biomass.[15] In the third stage (~420–700 °C), a slower decomposition is observed, as evident from the DTG curve with a less intense minimum in this zone, which can be assigned to the breakdown of lignin and char formation. At ~700 °C, the DTG curve approaches near zero, and the TGA curve flattens until 900 °C.[16] X-ray diffraction (XRD) analysis was conducted to understand the structural properties of the material. Fig. 1b confirms the predominant amorphous nature of both the materials, which is characterized by broad diffraction peaks at $2\theta = \sim 22°$ and $\sim 42°$; these peaks correspond to (002) and (100) planes for turbostratic carbon, respectively. Compared to BLC, BLC_KOH shows a shoulder peak at (100) plane, reflecting increased structural orderliness.[17]

The degree of graphitisation and structural defects in the activated carbon were systematically evaluated using Raman

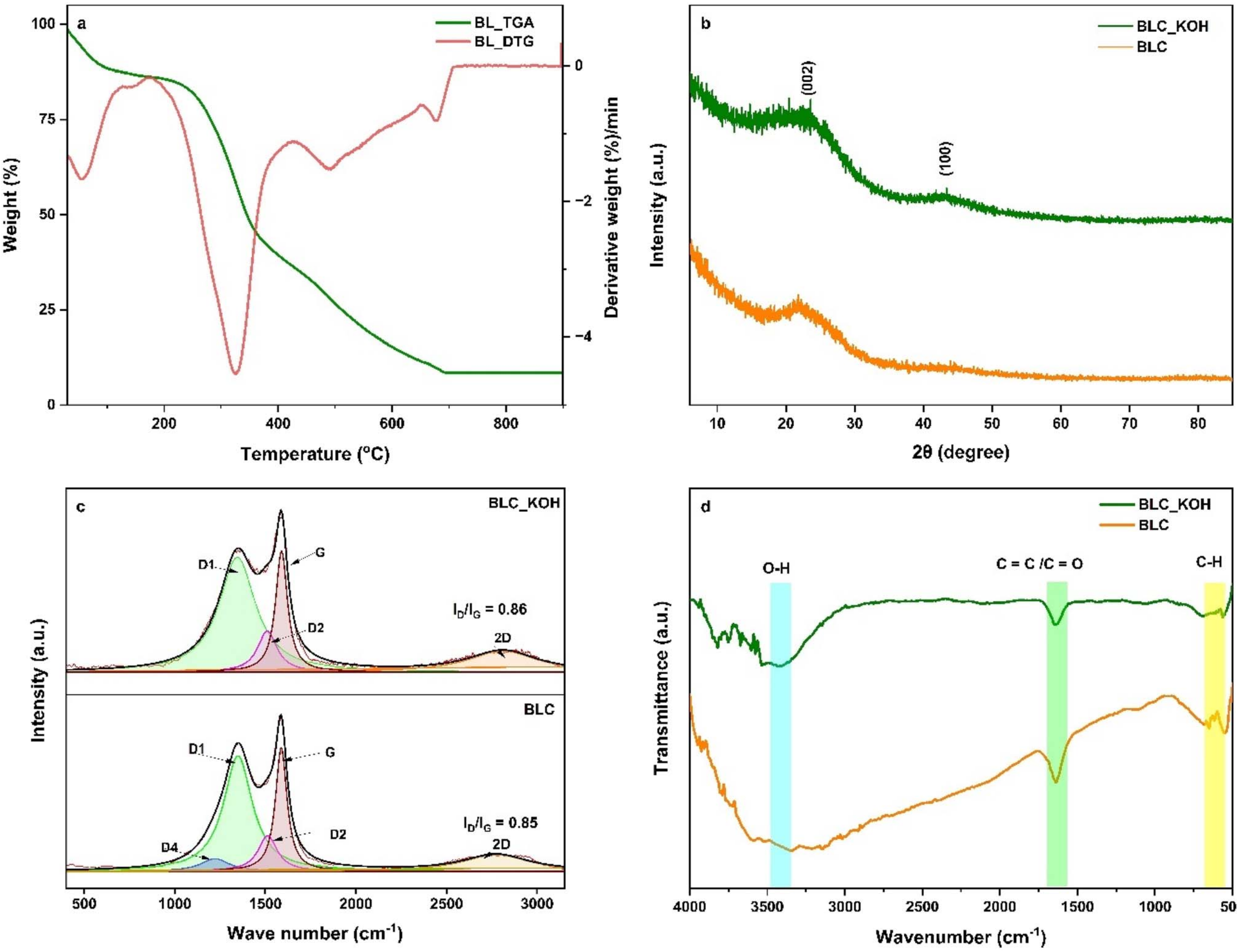

Fig. 1 (a) TGA and DTG plots, (b) XRD spectra, (c) Raman spectra and (d) FTIR spectra of BLC and BLC_KOH.

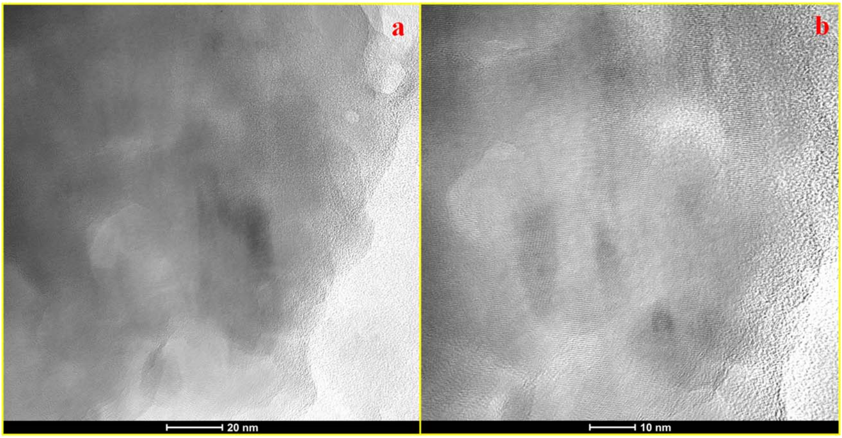

Fig. 2 (a) and (b) TEM images of BLC_KOH at different magnifications.

spectroscopy. As shown in Fig. 1c, the Raman spectra of both samples exhibit characteristic D and G bands at ~1359.41 cm^{-1} and ~1589.45 cm^{-1}, respectively, for BLC_KOH, and at ~1352.62 cm^{-1} and ~1587.27 cm^{-1} for BLC, respectively. The degree of disorder was quantified using the intensity ratio (I_D/I_G), which was calculated as 0.85 for BLC and 0.86 for BLC_KOH. The Raman spectra were deconvoluted to provide a detailed analysis of vibrational modes using Lorentzian line shapes, consistent with the reported literature for similar carbonaceous materials. The deconvoluted Raman spectra were characterised by multiple first-order bands (D1, D2, D4, and G) and a broad second-order band (2D). The D1 band arises from the defect-activated A_{1g} breathing mode of sp^2 aromatic rings, which serves as a primary indicator of structural disorder and lattice imperfections in the carbon framework.[18] The G band corresponds to the in-plane stretching vibration of C–C bonds (E_{2g} mode) in graphitic sp^2 carbon materials.[19] The D2 band is associated with lattice vibrations that correspond to the G band in the bulk sp^2 carbon framework. The D4 band arises as a result of lattice vibrations corresponding to mixed sp^2–sp^3 bonds.[20] A broad, weak second-order band appeared in the 2D region.

Molecular functional groups were identified by using FT-IR spectroscopy, as shown in Fig. 1d. Both samples exhibit a broad adsorption band between 3200 cm^{-1} and 3600 cm^{-1}, which is typically attributed to stretching vibrations of hydroxyl groups (O–H), and peaks at ~1640 cm^{-1} show the presence of stretching vibrations of C=C and C=O bonds. The peaks at ~650 cm^{-1} can be attributed to the C–H bending vibrations.[21] KOH-activated carbon shows a decrease in the intensity of the broad O–H band, which implies the removal of surface oxygen functional groups during KOH chemical activation owing to its dehydrating nature.[22,23]

TEM analysis, as shown in Fig. 2a and b, was performed to study the topographical and morphological characteristics of the KOH-treated activated carbon (BLC_KOH). The TEM images indicate a hybrid carbon framework comprised of amorphous regions and localised graphitic domains within the sample. The high-resolution image shows that the lattice fringes are not continuous over long distances. Such fragmented fringes are associated with a turbostratic carbon structure, where graphene layers are misaligned and lack long-range stacking order. Overall, the TEM analysis corroborates the structural conclusions derived from XRD and Raman spectroscopy, supporting the presence of a partially graphitized yet defect-rich carbon framework in BLC_KOH. The morphologies of both materials, as shown in Fig. 3a for BLC_KOH and Fig. 3c for BLC, show a porous nature, which plays an important role in energy storage systems. This honeycomb porous framework can be attributed to the carbonisation and chemical activation processes, which help to increase specific surface area (SSA). EDX analysis (as shown in Fig. 3b and d) reveals an increase in the carbon and a decrease in the oxygen content with KOH activation.

N_2 adsorption–desorption isotherm studies were conducted to understand the surface properties of the materials. Both materials exhibit a Type IV isotherm shape with a H4 hysteresis loop (as shown in Fig. 4a), which is characteristic of materials featuring both micropores and mesopores with a narrow slit shape.[24,25] At very low relative pressures, a sharp rise in adsorbed volume is observed, which can be attributed to micropore filling. In the relative pressure range from 0.1 to 0.4, a gentle slope is observed, which signifies multilayer adsorption on the mesopore walls. The KOH-activated material shows a higher uptake, indicating enhanced surface area and pore accessibility. At a relative pressure ($P/P_0 > 0.4$), both samples exhibit a H4 hysteresis loop, confirming the presence of slit-shaped mesopores, narrow pore channels where capillary condensation occurs, and an interconnected pore network. This is further confirmed by the pore-size distribution curve shown Fig. 4b. Compared with the BLC material, the KOH-activated material (BLC_KOH) at 700 °C exhibits a drastically increased specific surface area (S_{BET}) from 332.314 $m^2\ g^{-1}$ to 495.56 $m^2\ g^{-1}$, micropore area from 194.068 $m^2\ g^{-1}$ to 385.924 $m^2\ g^{-1}$, total pore volume from 0.355 $cm^3\ g^{-1}$ to 0.397 $cm^3\ g^{-1}$, and micropore volume from 0.118 $cm^3\ g^{-1}$ to 0.215 $cm^3\ g^{-1}$, as shown in Table 1.

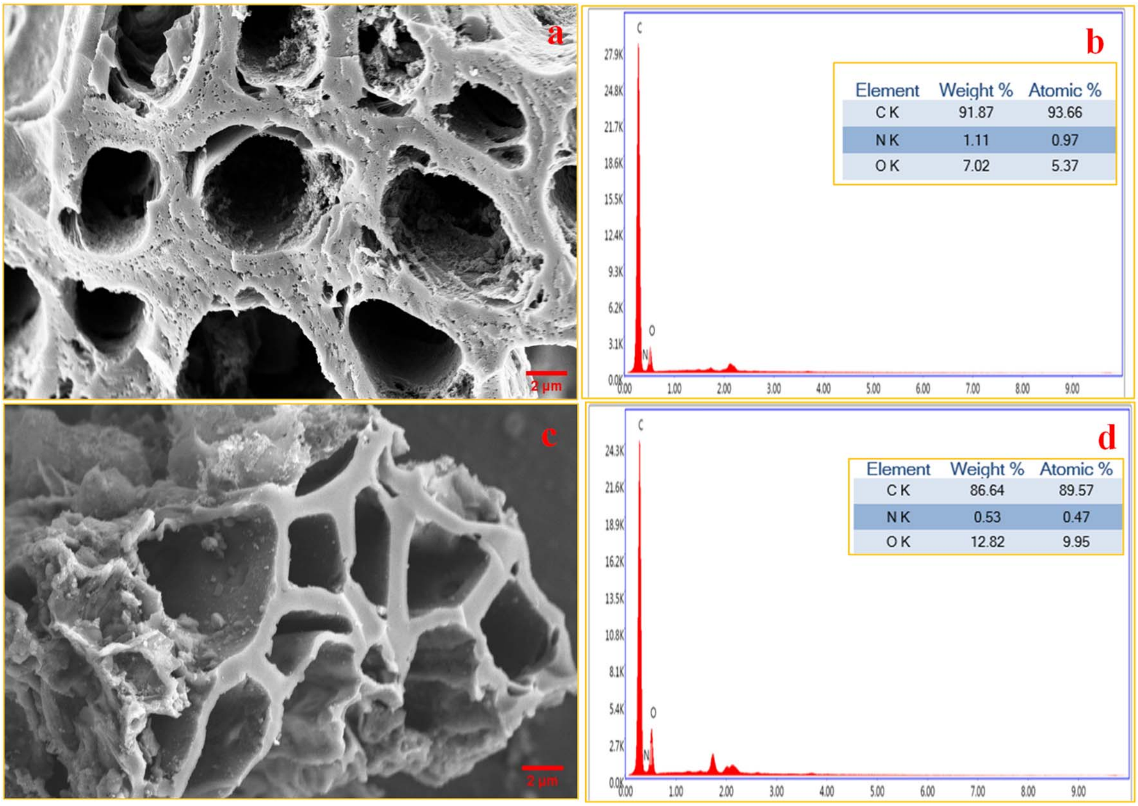

Element	Weight %	Atomic %
C K	91.87	93.66
N K	1.11	0.97
O K	7.02	5.37

Element	Weight %	Atomic %
C K	86.64	89.57
N K	0.53	0.47
O K	12.82	9.95

Fig. 3 (a) FESEM image of BLC_KOH, (b) EDX analysis of BLC_KOH, (c) FESEM image of BLC and (d) EDX analysis of BLC.

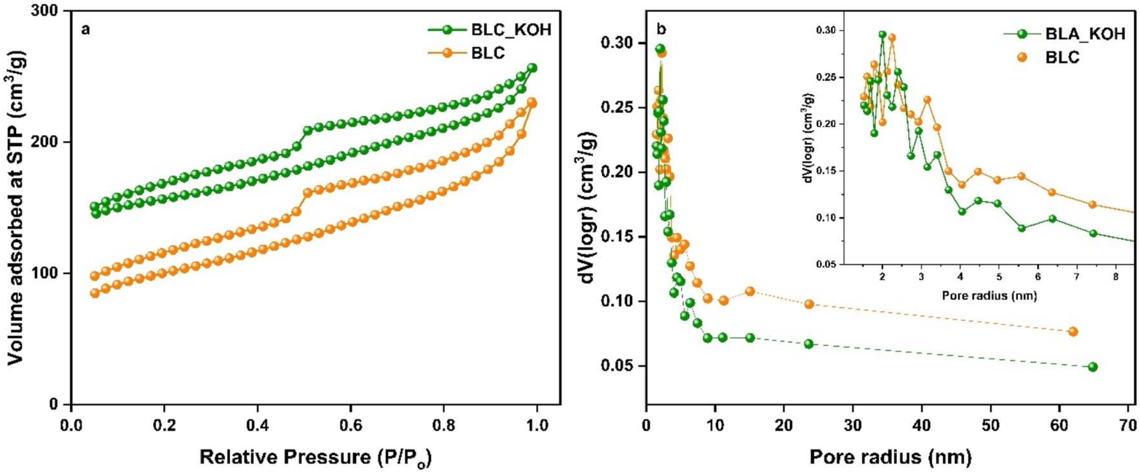

Fig. 4 (a) N_2 adsorption–desorption isotherms and (b) pore-size distribution curves of BLC_KOH and BLC.

XPS analysis was conducted to study the elemental composition and surface functional groups present in the BLC_KOH material. The XPS spectra, shown in Fig. 5a, confirm the presence of carbon (C 1s), nitrogen (N 1s), and oxygen (O 1s) in the derived material. The C 1s spectra is deconvoluted into four peaks at 284.5 eV (atomic conc. 54.7%), 286.0 eV (atomic conc. 22.3%), 288.7 eV (atomic conc. 17.4%), and 291.2 eV (atomic conc. 3.3%), as shown in Fig. 5b. The peak at 284.5 eV denotes the presence of sp^2-hybridised graphitic carbon (C–C) groups.[26] The peak at 286.0 eV can be assigned to C–O (alcohol/ether) or C–N groups. The peak at 288.7 eV can be assigned to O–C=O groups, and the peak at 291.2 eV (π–π^* satellite peak) indicates the presence of aromatic or graphitic domains in the carbon material.[27] The O 1s spectrum (Fig. 5c) is deconvoluted into three components at 532.1 eV (atomic conc. 81.2%), 533.36 eV (atomic conc. 12.7%) and 535.1 eV (atomic conc. 5%), each denoting different surface functional groups. The peak at 532.1 eV is attributed to carbonyl and quinone (C=O) groups,

Table 1 Textural properties of BLC and BLC_KOH

Material	Micropore area[a] (m^2 g^{-1})	Total surface area[b] (m^2 g^{-1})	Micropore volume[a] (cm^3 g^{-1})	Total pore volume[c] (cm^3 g^{-1})	Average pore size (nm)
BLC	194.068	332.314	0.118	0.3552	2.137
BLC_KOH	385.924	495.562	0.215	0.3971	1.603

[a] *t*-plot method. [b] BET method. [c] BJH method.

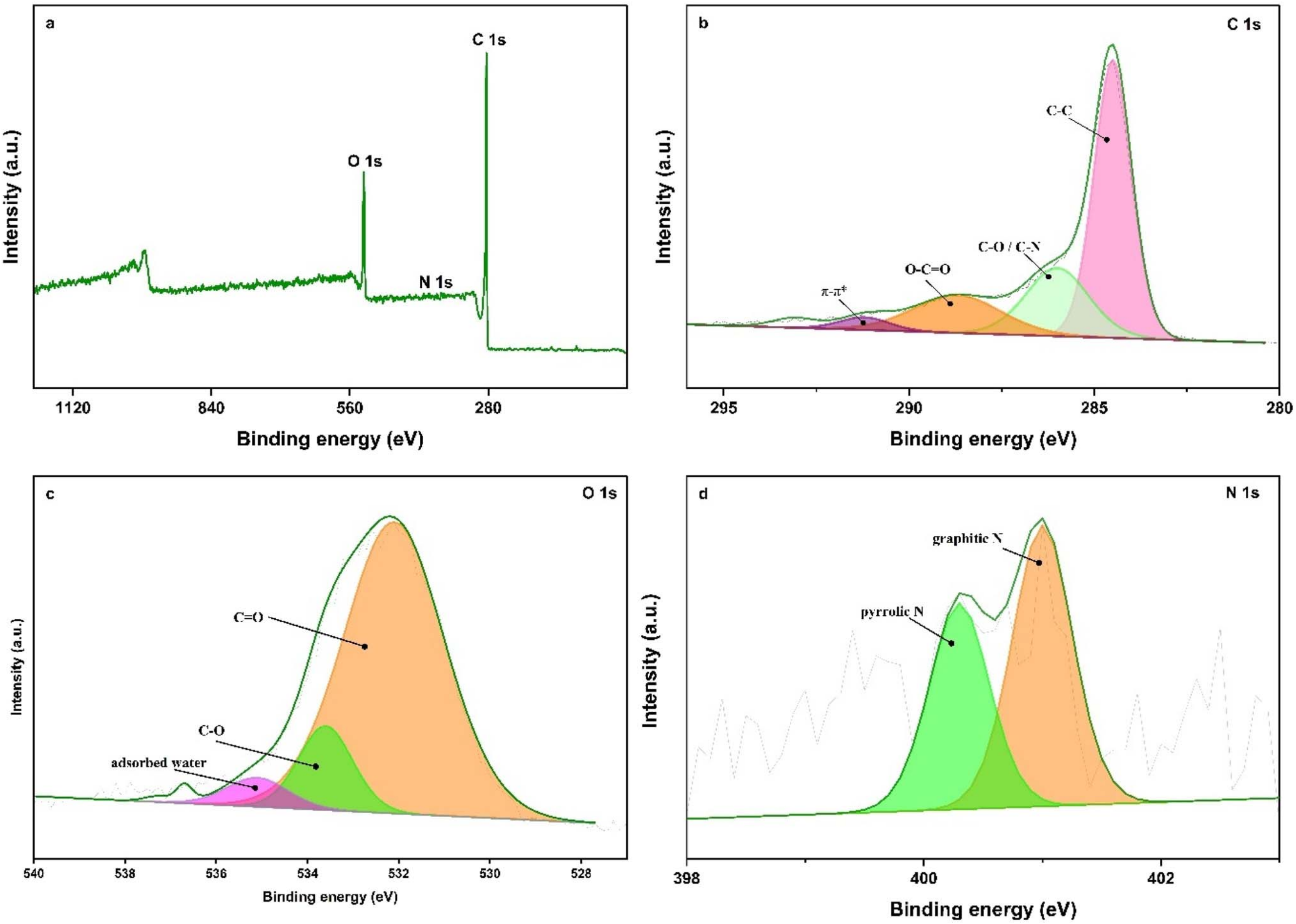

Fig. 5 XPS spectrum of BLC_KOH: (a) full spectrum and (b) C 1s, (c) O 1s and (d) N 1s spectra.

the peak at 533.6 eV is assigned to C–O–H or C–O–C groups,[28] and the peak at 535.1 eV is associated with chemisorbed water.[29] The N 1s spectrum is deconvoluted into two components, as shown in Fig. 5d: peak 1 at 400.3 eV (atomic conc. 42.3%) and peak 2 at 401.0 eV (atomic conc. 57.7%).[30] Pyrrolic N (N-5, 400.3 eV), found at the edges and defective sites in carbon layers, may provide additional active sites, which help in the adsorption of electrolyte ions, and graphitic N (N-Q, 401.00 eV) contributes to the wettability and electrical conductivity of the material.[31,32]

3.2 Electrochemical performance

Electrochemical performance was evaluated in the two-electrode symmetric configuration using 1 M Na_2SO_4 as the electrolyte with BLC_KOH as the electrode material. The charge-storage mechanism was studied using cyclic voltammetry (CV) with a scan rate of 5 mV s^{-1} to 100 mV s^{-1}. Fig. 6a shows a quasi-rectangular shape, which is characteristic of EDLCs with pseudocapacitive contributions. EDLCs store energy through ion adsorption at the electrode–electrolyte interface, creating a double layer.[33]

The CV curves were analysed further using the power law and Dunn method. The power law relationship, which relates current and scan rate (as shown in eqn (1) and (2)) in electrochemical analysis, reveals the underlying charge-storage mechanisms in energy storage materials:

$$i = av^b \tag{1}$$

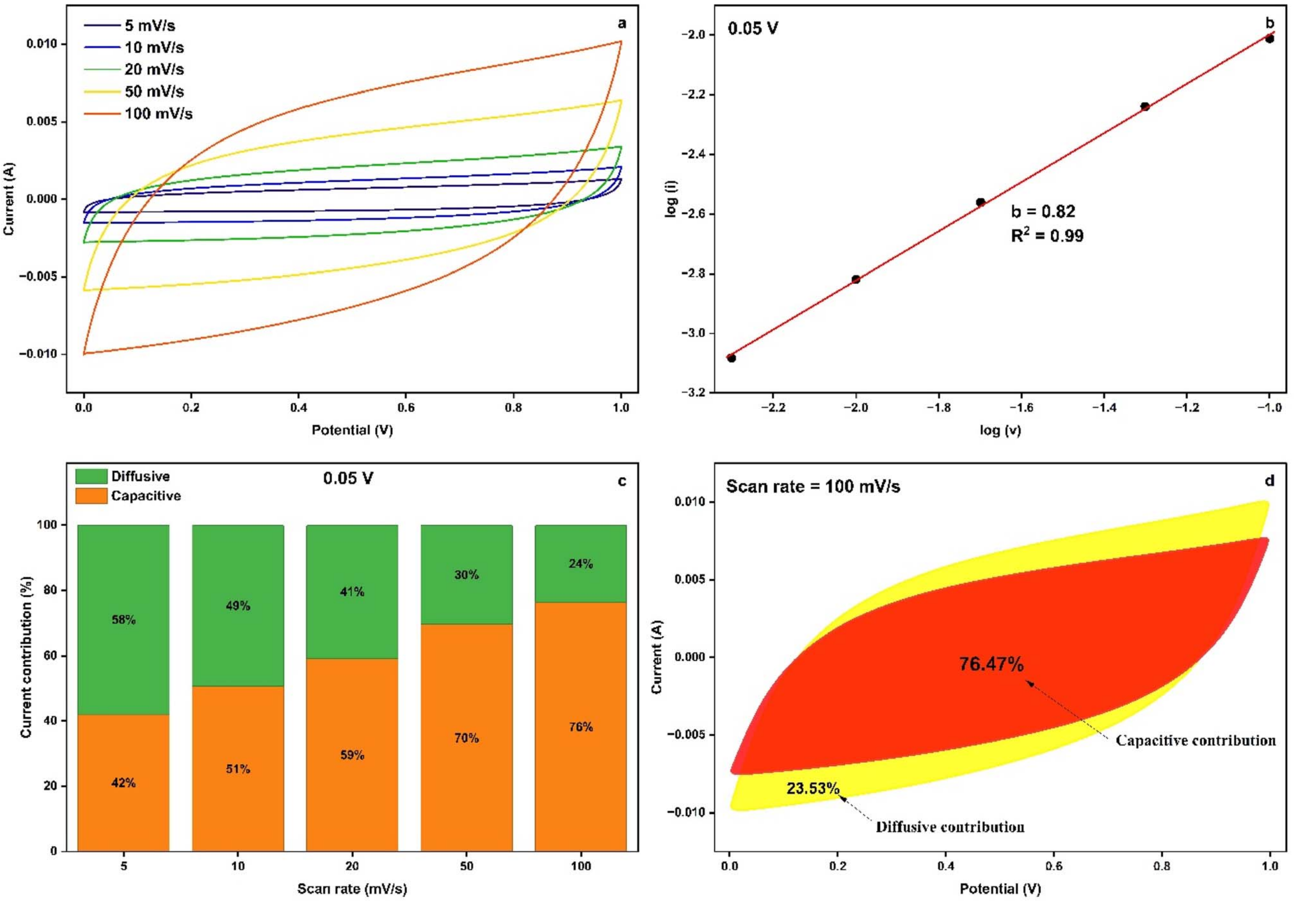

Fig. 6 (a) Cyclic voltammograms, (b) b-value at a potential of 0.05 V, (c) current contribution at 0.05 V, and (d) deconvoluted CV profile at 100 mV s^{-1}.

$$\log(i) = b\log(\nu) + \log(a) \tag{2}$$

where i is the peak current, ν is the scan rate, and 'a' and 'b' are constants. The slope of $\log(i)$ *vs.* $\log(\nu)$ provides a b-value. A b-value equal to 1 represents the ideal surface (capacitive) controlled charge-storage mechanism, and a b-value equal to 0.5 indicates a pure diffusion-controlled charge-storage mechanism. A b-value between 0.5 and 1.0 represents mixed charge-storage mechanisms.[34] From Fig. 6b, the observed b-values lie between 0.5 and 1, which indicate a mixed charge-storage mechanism. As the b-value is closer to unity, surface-dominated mixed behaviour can be observed. Additionally, Dunn analysis was performed using mathematical eqn (3) and (4)[35,36] to understand the contribution from different types of charge-storage mechanisms:

$$i(\nu) = k_1\nu + k_2\sqrt{\nu} \tag{3}$$

$$\frac{i(\nu)}{\sqrt{\nu}} = k_1\sqrt{\nu} + k_2 \tag{4}$$

where i is the current, $k_1\nu$ implies the capacitive current, and $k_2\sqrt{\nu}$ implies the diffusive current. The plot of $\frac{i(\nu)}{\sqrt{\nu}}$ *vs.* $\sqrt{\nu}$ provides k_1 (slope) and k_2 (y-intercept) values. The values of k_1 and k_2 were used to calculate capacitive current and diffusive current contributions, respectively. Fig. 6c and d show the capacitive and diffusive current contributions across different scan rates and the deconvoluted CV curve at a scan rate of 100 mV s^{-1}, respectively. It can be inferred that with increasing scan rate (5 mV s^{-1} to 100 mV s^{-1}), the contribution from the surface-controlled mechanism increases from 42% at 5 mV s^{-1} to 76% at 100 mV s^{-1}. The transition from the diffusion-controlled mechanism to the surface-controlled mechanism can be attributed to the kinetic and mass-transport limitations that arise at higher scan rates.[35]

Galvanostatic charge–discharge (GCD) testing was performed to understand the practical performance of the supercapacitor at different current densities (0.2 A g^{-1} to 1 A g^{-1}) with the potential range of 0–1 V. Fig. 7a reveals a deviation from the triangular shape that is characteristic of ideal capacitive behaviour, indicating mixed EDLC and pseudocapacitive behaviour.[37] At a current density of 0.2 A g^{-1}, the BLC_KOH electrode showed a specific capacitance of 561.22 F g^{-1}. The electrochemical performance observed for BLC_KOH electrode is benchmarked against that observed for existing biomass-derived activated carbon supercapacitors, as summarized in Table 2. This higher specific capacitance can be attributed to the specific surface area and hierarchical and interconnected

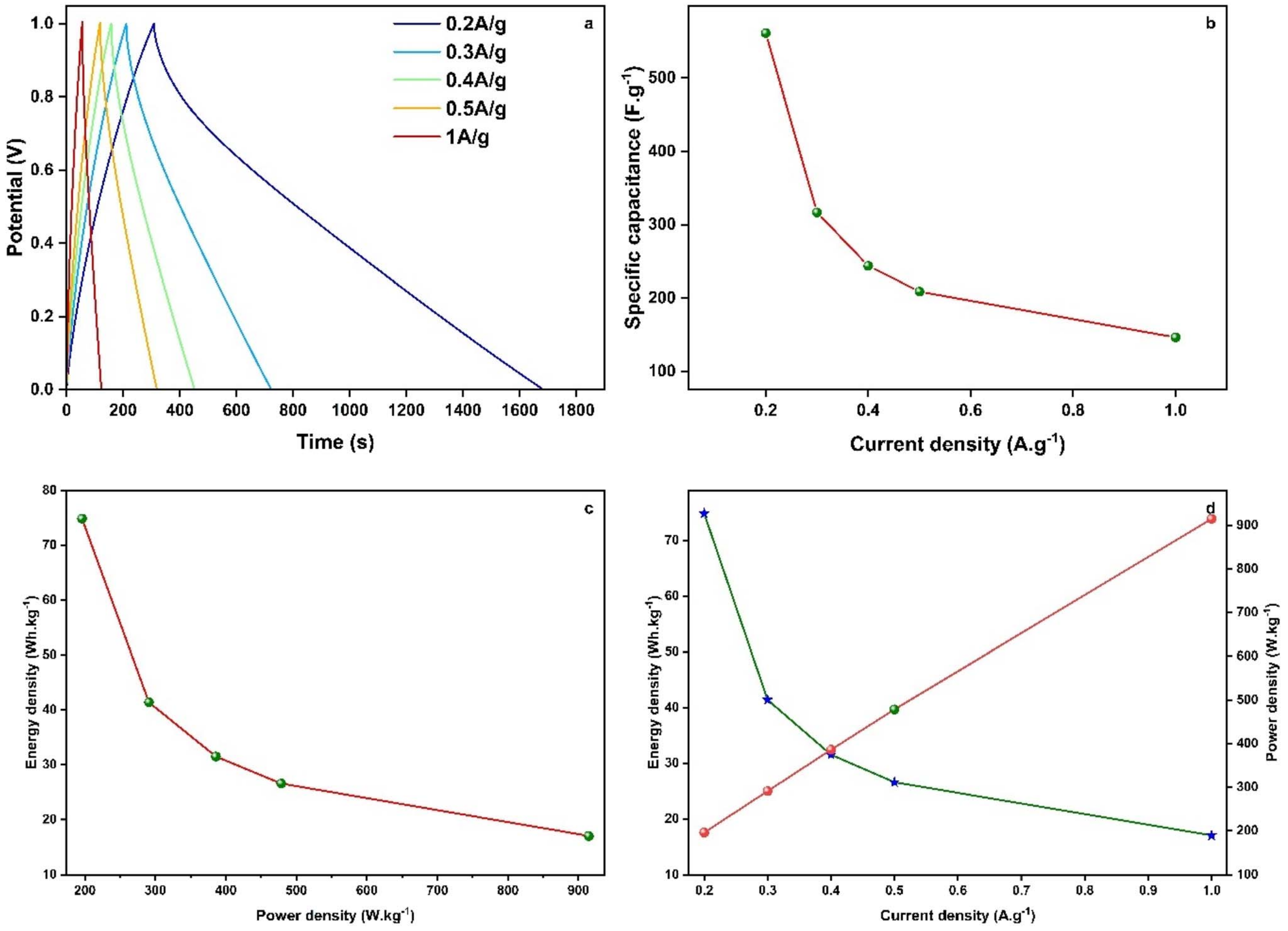

Fig. 7 (a) GCD plots, (b) specific capacitance *vs.* current density plot, (c) Ragone plot and (d) current density *vs.* energy density and power density plot.

pore size distribution, which facilitate ion transport, while pseudo-capacitance contribution can be attributed to the presence of heteroatom species such as oxygen and nitrogen. An increase in current density (0.2 A g^{-1} to 1 A g^{-1}) results in a reduction of the specific capacitance, as depicted in Fig. 7b. This declining capacitance at higher currents arises from kinetic and mass transport limitations that restrict ions from accessing the electrode's micropores and mesopores, which lead to incomplete utilisation of specific surface area and to ohmic (I_R) drop increases that reduces the usable potential window and discharge time.[38]

The Ragone plot (Fig. 7c) was obtained by calculating the energy density and power density for the BLC_KOH electrode, which illustrates a good electrochemical performance. It was observed that energy density decreases as the power density increases, which is a universal feature for all practical electrochemical energy storage devices that can be attributed to kinetic and mass transport limitations and an I_R drop. Fig. 7d shows the energy density-power density relationship, which demonstrates the fundamental trade-off characteristic of supercapacitor performance, where the energy density decreases from 75 to 17 Wh kg^{-1} while the power density increases from

Table 2 Electrochemical performance comparison of biomass-derived activated carbons

Biomass	Electrolyte	Current density (A g^{-1})	Specific capacitance (F g^{-1})	Ref.
Acacia tree bark	1 M Na_2SO_4	1	191	39
Cashew nut shells	1 M Na_2SO_4	1	214	40
Tea waste	1 M Na_2SO_4	1	138	41
Empty fruit bunches	6 M KOH	0.1	346	42
Juncus effuses	6 M KOH	0.5	233	43
Chinese date	1 M Na_2SO_4	0.5	164	44
Bamboo	6 M KOH	0.5	179	45
Rice husk	6 M KOH	0.1	315	46
Bacillus subtilis	1 M H_2SO_4	0.2	305	47
Popcorn	6 M KOH	0.2	348	48
Pistachio shells	1 M H_2SO_4	0.5	188	49
Ficus benghalensis (banyan tree) leaves	1 M Na_2SO_4	0.2 0.5	561.22 208.98	This work

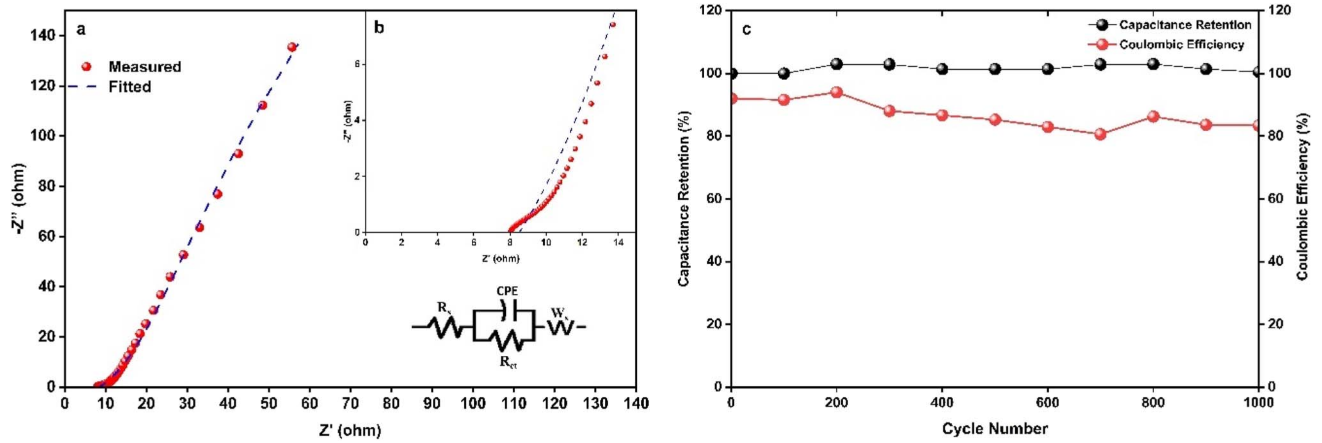

Fig. 8 (a and b) Electrochemical impedance spectra and (c) cyclic stability of BLC_KOH.

196 to 915 W kg^{-1} as the current density rises from 0.2 to 1.0 A g^{-1}. An electrochemical impedance spectroscopy (EIS) study was conducted to obtain the Nyquist plot (0.01 Hz to 1 MHz, amplitude 10 mV), as shown in Fig. 8a. The EIS data were fitted to the equivalent circuit model, shown in the inset of Fig. 8a, using the ZSimp software to quantify resistive components. The fitted parameters correspond to a total resistance of 9.459 Ω, an R_s of 7.959 Ω, and a charge-transfer resistance (R_{ct}) of 0.002 Ω. The nearly vertical linear pattern in the low-frequency region indicates good capacitive behaviour with rapid ion diffusion and efficient charge transfer, and the presence of a small semicircle in the high-frequency region indicates a very well-formed double-layer capacitance, which reflects rapid interfacial kinetics in the BLC_KOH electrode.[50] Finally, the BLC_KOH electrode was subjected to long-term GCD testing at a current density of 4 A g^{-1} to understand the durability of the electrode. The results (as shown in Fig. 8b) reveal an outstanding ∼99.99% capacity retention even after 1000 cycles and a coulombic efficiency of 83.2%, which demonstrates their superior cycling stability and reliability. The findings obtained through different electrochemical characterisation techniques collectively validate a better electrochemical performance, highlighting their potential application in high-performance devices such as electric vehicle regenerative braking, grid frequency regulation, and consumer electronics.

4 Conclusions

This current research work successfully synthesised activated carbon from *Ficus benghalensis* leaves by employing a dual approach of physical activation and chemical activation using KOH at 700 °C. Physicochemical and morphological characterisations revealed the amorphous nature of the activated carbon (BLC_KOH), with a well-connected hierarchical porous structure, a specific surface area (S_{BET}) of 495.56 m^2 g^{-1}, and the presence of several functional groups. These combined features promote ion transport and charge accumulation, which leads to better electrochemical performance. Electrochemical characterisation revealed a *b*-value of 0.82 at 0.05 V, a surface-controlled mechanism (76%) at a scan rate of 100 mV s^{-1}, and a specific capacitance of 561.22 F g^{-1} at a current density of 0.2 A g^{-1}. An outstanding cycling stability was achieved, with a capacity retention of ∼99.99% and a coulombic efficiency of 83.2% after 1000 charge–discharge cycles at a higher current density of 4 A g^{-1}. Together, these results demonstrate that BLC_KOH is a promising electrode material for high-performance and sustainable energy storage solutions.

Conflicts of interest

There are no conflicts to declare.

Data availability

All the necessary and sufficient data supporting the findings of this study are provided in the manuscript. Any additional data relevant to the findings are available from the corresponding author upon reasonable request.

Supplementary information (SI) is available. See DOI: https://doi.org/10.1039/d5ra09628f.

Acknowledgements

The authors acknowledge the Central Research Facility, National Institute of Technology Karnataka (NITK), for providing access to the research facilities. We are grateful to the National Institute of Technology Karnataka, for the institutional support and comprehensive library resources that facilitated this research work.

References

1 S. S. Hegde and B. R. Bhat, *RSC Adv.*, 2024, **14**, 8028–8038.
2 K. Dissanayake and D. Kularatna-Abeywardana, *J. Energy Storage*, 2024, **96**, 112563.
3 C. Yuan, H. Xu, S. A. El-khodary, G. Ni, S. Esakkimuthu, S. Zhong and S. Wang, *Fuel*, 2024, **362**, 130795.
4 P. Simon and Y. Gogotsi, *Nat. Mater.*, 2008, **7**, 845–854.

5 J. Mitali, S. Dhinakaran and A. A. Mohamad, *J. Power Sources*, 2026, **668**, 239306.

6 C. Yang, T. Sun, W. Wang, Y. Li, Y. Zhang and M. Zha, *Renew. Sustain. Energy Rev.*, 2024, **198**, 114389.

7 G. Lee, J. Song, J. Han, Y. Lim and S. Park, *Energy*, 2023, **283**, 128745.

8 Z. Wang, J. Li, C. Hu, X. Li and Y. Zhu, *J. Energy Storage*, 2024, **75**, 109432.

9 S. Iijima, *Nature*, 1991, **354**, 56–58.

10 K. S. Novoselov, A. K. Geim, S. V. Morozov, D. Jiang, Y. Zhang, S. V. Dubonos, I. V. Grigorieva and A. A. Firsov, *Science*, 2004, **306**, 666–669.

11 D. M. Saju, R. Sapna, U. Deka and K. Hareesh, *J. Power Sources*, 2025, **647**, 237302.

12 S. Narayanaperumal, D. Divakaran, M. K. Singh, M. R. Sanjay, S. Siengchin and I. Suyambulingam, *Int. J. Biol. Macromol.*, 2024, **277**, 134394.

13 P. Singh, J. Dhankhar, R. K. Kapoor, D. Kumar, S. Bhatia, A. Al-Harrasi and A. Sharma, *J. Appl. Pharm. Sci.*, 2023, **13**, 059–082.

14 M. C. Cheng, Y. S. Chang, D. C. Tsai, Y. L. Huang and F. S. Shieu, *Fuel*, 2025, **387**, 133790.

15 R. K. Singh, D. Pandey, T. Patil and A. N. Sawarkar, *Bioresour. Technol.*, 2020, **310**, 123464.

16 M. Carrier, A. Loppinet-Serani, D. Denux, J. M. Lasnier, F. Ham-Pichavant, F. Cansell and C. Aymonier, *Biomass Bioenergy*, 2011, **35**, 298–307.

17 H. Li, Y. Ma, Y. Wang, C. Li, Q. Bai, Y. Shen and H. Uyama, *Renewable Energy*, 2024, **224**, 120144.

18 A. Bello, F. Barzegar, M. J. Madito, D. Y. Momodu, A. A. Khaleed, T. M. Masikhwa, J. K. Dangbegnon and N. Manyala, *Electrochim. Acta*, 2016, **213**, 107–114.

19 A. Sadezky, H. Muckenhuber, H. Grothe, R. Niessner and U. Pöschl, *Carbon*, 2005, **43**, 1731–1742.

20 D. Momodu, M. Madito, F. Barzegar, A. Bello, A. Khaleed, O. Olaniyan, J. Dangbegnon and N. Manyala, *J. Solid State Electrochem.*, 2016, (21), 859–872.

21 P. P. Mon, P. P. Cho, S. S. Hegde, S. Dobhal, A. Ramesh, K. K. Garlapati, S. K. Martha and C. Subrahmanyam, *Energy Fuels*, 2026, **40**(7), 3904–3916.

22 Z. Guo, X. Han, C. Zhang, S. He, K. Liu, J. Hu, W. Yang, S. Jian, S. Jiang and G. Duan, *Chinese Chem. Lett.*, 2024, **35**, 109007.

23 N. A. M. Barakat, M. S. Mahmoud and H. M. Moustafa, *Sci. Rep.*, 2024, **14**, 1–13.

24 W. Gao, Y. Shi, Y. Zhou, J. Jia and S. Chen, *Sci. Rep.*, 2025, **15**, 1–17.

25 M. Thommes, K. Kaneko, A. V. Neimark, J. P. Olivier, F. Rodriguez-Reinoso, J. Rouquerol and K. S. W. Sing, *Pure Appl. Chem.*, 2015, **87**, 1051–1069.

26 H. Cao, X. Peng, M. Zhao, P. Liu, B. Xu and J. Guo, *RSC Adv.*, 2018, **8**, 2858–2865.

27 X. Chen, X. Wang and D. Fang, *Fullerenes, Nanotub. Carbon Nanostructures*, 2020, 1048–1058.

28 K. Tian, J. Wang, L. Cao, W. Yang, W. Guo, S. Liu, W. Li, F. Wang, X. Li, Z. Xu, Z. Wang, H. Wang and Y. Hou, *Nat. Commun.*, 2020, **11**, 1–10.

29 G. Ketteler, P. Ashby, B. S. Mun, I. Ratera, H. Bluhm, B. Kasemo and M. Salmeron, *J. Phys. Condens. Matter*, 2008, **20**, 184024.

30 C. Liu, Q. Lu, J. Qu, W. Feng, A. Thomas, Y. Li, I. G. G. Martinez, C. Pan and D. Mikhailova, *Small*, 2024, **20**, 2311253.

31 Y. R. Zhao, C. C. Liu, Q. Q. Lu, A. Omar, X. J. Pan and D. Mikhailova, *New Carbon Mater.*, 2022, **37**, 875–897.

32 F. Liu, J. Liu, J. He, J. Niu, P. Feng and X. Chuan, *J. Energy Storage*, 2025, **134**, 118210.

33 P. Adoor, S. S. Hegde, B. R. Bhat, S. N. Yethadka and R. Yeenduguli, *ACS Omega*, 2023, **8**, 46640–46652.

34 P. A, S. S. Hegde, B. Ramachandra Bhat, C. Yadav K, S. Chakraborty, A. Ravikumar, S. D. George, Y. N. Sudhakar and R. Y, *Phys. Scr.*, 2024, **99**, 105922.

35 J. Li, X. Wang, J. Tang, S. Wang and S. Sheng, *Biomass Bioenergy*, 2025, **202**, 108188.

36 K. M. Albalawi, M. Al-Dossari, A. M. Saeedi, R. H. Althomali, G. F. B. Solre, M. Sadiq and S. U. Asif, *J. Energy Storage*, 2024, **104**, 114576.

37 S. S. Hegde and B. R. Bhat, *J. Energy Storage*, 2024, **76**, 109818.

38 N. Blomquist, T. Wells, B. Andres, J. Bäckström, S. Forsberg and H. Olin, *Sci. Rep.*, 2017, **7**, 39836.

39 C. Pratheep, K. Ramesh, M. Kiruthiga, M. Saravanan, M. Sugirtha and K. Suridha, *Asian J. Chem.*, 2024, **36**, 2659–2665.

40 P. Merin, P. Jimmy Joy, M. N. Muralidharan, E. Veena Gopalan and A. Seema, *Chem. Eng. Technol.*, 2021, **44**, 844–851.

41 X. Song, X. Ma, Y. Li, L. Ding and R. Jiang, *Appl. Surf. Sci.*, 2019, **487**, 189–197.

42 F. Ngosong, C. N. Anyanwu and I. S. Eze, *Next Mater.*, 2026, **11**, 101640.

43 R. Ye, J. Cai, Y. Pan, X. Qiao and W. Sun, *Diam. Relat. Mater.*, 2020, **105**, 107816.

44 Y. L. Zhang, C. Sun and Z. S. Tang, *Diam. Relat. Mater.*, 2019, **97**, 107455.

45 Z. M. Abdulhamid, A. C. Lokhande, A. H. Emwas, D. Choi, Y. A. Samad, K. Polychronopoulou and D. H. Anjum, *Environ. Technol. Innov.*, 2026, **41**, 104681.

46 S. Dong, X. He, H. Zhang, X. Xie, M. Yu, C. Yu, N. Xiao and J. Qiu, *J. Mater. Chem. A*, 2018, **6**, 15954–15960.

47 H. Zhu, J. Yin, X. Wang, H. Wang and X. Yang, *Adv. Funct. Mater.*, 2013, **23**, 1305–1312.

48 J. Hou, K. Jiang, R. Wei, M. Tahir, X. Wu, M. Shen, X. Wang and C. Cao, *ACS Appl. Mater. Interfaces*, 2017, **9**, 30626–30634.

49 Y. Yardım and C. Saka, *J. Anal. Appl. Pyrolysis*, 2026, **195**, 107634.

50 S. Subraya Hegde and B. Ramachandra Bhat, *Fuel*, 2024, **371**, 131999.